

RSC Advances



This is an *Accepted Manuscript*, which has been through the Royal Society of Chemistry peer review process and has been accepted for publication.

Accepted Manuscripts are published online shortly after acceptance, before technical editing, formatting and proof reading. Using this free service, authors can make their results available to the community, in citable form, before we publish the edited article. This *Accepted Manuscript* will be replaced by the edited, formatted and paginated article as soon as this is available.

You can find more information about *Accepted Manuscripts* in the [Information for Authors](#).

Please note that technical editing may introduce minor changes to the text and/or graphics, which may alter content. The journal's standard [Terms & Conditions](#) and the [Ethical guidelines](#) still apply. In no event shall the Royal Society of Chemistry be held responsible for any errors or omissions in this *Accepted Manuscript* or any consequences arising from the use of any information it contains.

Amorphous apatite thin film formation on a biodegradable Mg alloy for bone regeneration: Strategy, characterization, biodegradation, and *in vitro* cell study

Hamouda M. Mousa^{1,2,3}, Kamal H. Hussein^{4,5}, Ahmed A. Raslan⁶, Joshua Lee¹,
Heung M. Woo^{4,5}, Chan Hee Park^{1,3*}, and Cheol Sang Kim^{1,3*}

¹Department of Bionanosystem Engineering, Chonbuk National University, Jeonju, Jeonbuk 561-756, Republic of Korea.

²Division of Mechanical Design Engineering, Chonbuk National University, Jeonju, Jeonbuk 561-756, Republic of Korea.

³Department of Engineering Materials and Mechanical Design, Faculty of Engineering, South Valley University, Qena 83523, Egypt.

⁴Stem Cell Institute, Kangwon National University, Chuncheon, Gangwon, Republic of Korea.

⁵College of Veterinary Medicine, Kangwon National University, Chuncheon, Gangwondo, Republic of Korea.

⁶Department of Systems Immunology, College of Biomedical Science, Kangwon National University, Chuncheon, Gangwondo, Republic of Korea.

*Corresponding authors:

Tel: +82 63 270 4284, Fax: +82 63 270 2460

chskim@jbnu.ac.kr (Cheol Sang Kim)

biochan@jbnu.ac.kr (Chan Hee Park)

Abstract

Bioactive films with nanoplates structure were prepared on the surface of biodegradable AZ31B magnesium (Mg) alloy via anodization in simulated body fluid (SBF) as electrolyte to control Mg biodegradability and improve surface bioactivity. The effect of the electrolyte temperature and pH values on the formation of the biomimetic film were studied. The electrolyte was set at three different temperatures of 37, 50, and 80 °C, with pH values ranged from 7.4 to 8 for the lower electrolyte temperature and 11.5 - 12 for the two higher levels of temperature. The apatite films on the different samples were characterized using X-ray diffraction spectroscopy (XRD), field emission scanning electron microscopy (FE-SEM), EDS element mapping, X-ray photon spectroscopy (XPS), and FTIR spectrum. Water contact angle of the different surfaces were evaluated, moreover, the corrosion behavior of the different samples were studied using electrochemical potentiodynamic DC, electrochemical impedance spectroscopy (EIS) , and immersion tests. The human fetal-osteoblast cell line hFOB 1.19 was used in a cell culture test, the biological response and cell function were evaluated *in vitro* using DNA and PCR. The decomposition of the apatite film formation was affected by the anodization electrolyte temperature resulted an amorphous structure. It is observed that the apatite structure has nanoplates at electrolyte temperature (37 to 50) °C and had a tendency to disappear at 80 °C.

Keywords

Magnesium alloy, Anodized film, Biomimetic, SBF, biocompatibility, bone tissue engineering

1. Introduction

Magnesium (Mg) is the fourth most abundant element in the human body and essential for the regulation of muscle contraction and human metabolism. It has the potential to be used in bone fixation as screw, and joint plates, as well as vascular stent. Mg characterized with its light weight, density that is close to that of natural bone at 1.74 g/cm^3 , and good mechanical properties^{1,2}. On the other hand, Mg and its alloys are sensitive to corrosion in a biological environment. It has a high rate of corrosion and a low bioactivity which are particularly challenging problems that limit its clinical application. To overcome such limitation study of Mg surface by different surface modification is the essential for most researchers³. The corrosion product of Mg in physiological media is not harmful to surrounding tissue, moreover, it is expected to be completely degraded in a physiological environment^{4, 5}. Surface modification of metallic implants is a suitable and popular strategy to improve the bioactivity of Mg to retard its degradation thus a new tissues completely healed and prevent it against inflammation occurrence in the surrounding tissue⁶. Different kind of techniques were employed as a surface modification to Mg and its alloys in order to improve physiochemical properties such as electrodepositing⁷, ions plating⁸, microarc oxidation⁹, sol-gel coatings¹⁰, and Anodization¹¹. Among them anodization is a very attractive and traditional way to control and protect metals against high corrosion rate as well as to improve the biocompatibility of Mg by using a proper electrolyte^{12, 13}. During anodization, Mg tends to form oxide layer on its surface according to the following reaction $\text{Mg} + \text{O}_2 \rightarrow \text{MgO}$. The resulting oxide layer have diverse properties functional properties depending on the chemical composition of the electrolyte¹⁴. Anodization has a unique properties such as increase the film thickness, hardness¹⁵, wear resistance¹⁶, corrosion resistance¹⁷, mechanical properties¹⁴, and good adhesion on the metal surface¹⁸. The resulted improvement

depend mainly on different parameters of anodizing such as applied voltage, time, current, and electrolyte composition^{15, 19}. The porosity of the anodized film consider as a proper way to avoid a mechanical mismatching in Mg implant and host bone²⁰.

Bioceramics apatite have excellent biocompatibility and considered as the most promising materials for bone repair since the appropriate cellular response to bioceramics surfaces is essential for bone tissue regeneration and characterized by protein adsorption^{21, 22}. Once bioceramics are in contact with a living body, the proteins present in the surrounding body fluids will be adsorbed onto their surfaces, and thereafter, cellular attachment and proliferation occur²³. As a result, protein adsorption plays a vital role during bone tissue regeneration^{24, 25}. Different studies was employed for Mg coating using HA to improve surface properties such as corrosion resistance^{26, 27} and bone implant²⁸. Hydroxyapatite (HA) ceramics coated on the metallic implants could improve the bioactivity of implant surface, and this resulted in osteoconduction, which is a tissue response in which bone tends to grow, engages with the coating, and forms a strong mechanical interface²⁹⁻³¹.

Simulated body fluid (SBF) with a precipitation of supersaturated calcium phosphate (Ca-P) has found extensive research interest due to the formation of bone like apatite³²⁻³⁴. The formation of amorphous apatite film promoted by an increase in pH of SBF solution³⁴. SBF temperature found to has a great effect on the bicarbonate deposition rate in SBF solution subsequently increase the pH value, especially in higher values³⁵. The formation of apatite deposits onto Mg alloys to enhance their corrosive resistance and their biocompatibility have been performed by soaking in SBF at room temperature for 5 days following by one days sealing with NaOH³⁶. In this study, biomimetic apatite film was formed using SBF solution via anodization in one step under different electrolyte temperature within 10 min at 40 V and 40 mA. The resulted Ca-P

apatite film with amorphous structure on the Mg alloy surface is accelerated by means of applied voltage over a short period of time comparing to the long time soaking in previous works^{35,37,38}. The effect of the electrolyte temperature on the biomimetic anodized film formation was investigated at 37 °C and 50 °C and at higher values of 80 °C with respect to the physiochemical properties of the AZ31B Mg alloy as well as the biological response through an *in vitro* study. The anodized film was found to mimic the bone apatite structure/composition and subsequently increase bone osteointegration, and different nano- structure formation was growth at cell culture media with nanoplates similar to that of bone.

2. Materials and methods

2.1 Sample preparation

Commercially available AZ31B Mg alloy (Alfa Aesar Company, South Korea) was purchased with a chemical composition as shown in **Table 1**. The substrate samples were cut using electric discharge machine (EDM) at dimensions of 12 mm × 12 mm and a thickness of 6.35 mm, thereafter, mechanically polished with SiC paper with successively finer roughness of up to 2000 grit. Finally, the samples were ultrasonically cleaned in acetone followed by cleaning in distilled water and dried in warm air.

2.2 Preparation of the anodization process

The anodization cell was composed of AZ31B Mg alloy as an anode and a platinum wire network as a cathode. The anodization process was carried out in SBF solution at different temperatures of 37, 50, and 80 °C at constant voltage of 40 V and current of 40 mA for 10 min under agitation with a magnetic stirrer at 120 rpm to maintain the electrolyte with a homogenous temperature. The pH value of the electrolyte was initially 7.4 and then reached 11.5 after the temperature increased to 50 °C and 80 °C. A DC power supply (IT6723H 300V/10A/850W) was

connected with a GP-7202GT, INTEC machine to control the anodization time during the process. The SBF solution was prepared as follows. Commercially available Hank's balanced salt (Aldrich, H2387-1L) was dissolved in 1 L of distilled water followed by the addition of MgSO_4 (0.097 g), NaHCO_3 (0.350 g), and CaCl_2 (0.185 g) to simulate the ions concentration in human blood plasma **Table 2**.

2.3 Surface characterization

The surface morphology of the anodized samples was characterized using a field emission scanning electron microscope (SU-70 SCHOTY type, HITACHI) with an electron beam of 0.5 nm at 15 kV. The phase composition and the crystallinity were obtained by using a Rigaku X-ray diffractometer (XRD, Rigaku, Japan) with Cu Ka ($k = 1.540 \text{ \AA}$) radiation over a Bragg angle ranging from 5 to 90 degree. The elemental composition of the anodized film in the outer layer was investigated using X-ray photoelectron spectroscopy (XPS), and aluminum (Al) was used as the anode material of the Thermo/K-Alpha ESCA System. Fourier Transform Infrared Spectrometer (FT-IR), (Perkin Elmer® Spectrum™ GX systems) Spectrum was used to check different functional groups on the anodized samples in the range of 400 to 4000 cm^{-1} . The hydrophobicity of the surface of the Mg alloy substrate and the anodized film surface was measured using a standard DPRO imaging device to measure the water contact angle.

2.4 Corrosion measurements

A ZIVE SP1 potentiostat /galvanostat /EIS device was used to carry out the electrochemical corrosion test. The electrochemical measurements were conducted with a conventional three-electrode system in an electrochemical cell composed of Mg samples and platinum plate working as working electrode and counter electrode, respectively, and a saturated Ag/AgCl in KCl as a reference electrode. The experiment was performed at 0.5 mV scan rate with initial and

final potentials are 3.0 and 1.5 V, respectively. The corrosion test was evaluated in SBF solution at 37 ± 0.5 °C, and electrochemical impedance spectroscopy (EIS) test was conducting in a frequency range from 100 kHz to 0.01 Hz with 10 points/decade at open circuit potential (OCP). The amplitude of the sinusoidal potential was of 10 mV with respect to the OCP. The area of the specimen exposed to the solution was 0.875 cm^2 , and three duplicate samples were measured for each sample group to control the experimental scattering. To check the corrosion products the different samples were immersed 12-well culture plate with alpha- MEM media with presence of MC3T3-E1 cells with 3×10^4 cells/well for three days, the samples were covered with media thereafter, samples morphology were checked with SEM. Immersion test of the different samples was evaluated to enhance the weight loss of the samples after 5, 10, and 15 days in SBF solution at 37 °C and 120 rpm shaking, samples weight were measured before and after immersion test, the corrosion products were removed using 200 g/l CrO_3 modified with the addition of 10 g/l AgNO_3 ³⁹.

2.5 Cell culture

Human fetal-osteoblast cell line, HFOB 1.19 were cultured in a 1 : 1 mixture of Ham's F12 and DMEM supplemented with 10% fetal bovine serum (FBS; Hyclone, Logan, UT, USA), 2.5 mM L-glutamine (Gibco, Grand Island, NY, USA) and 1% P/S in a humidified incubator at 34 °C and 5% CO_2 . The cells were harvested via trypsinization at a 70% confluence and were then used for further experiments. Extracts of different samples were prepared in a serum-free 1: 1 mixture of Ham's F12 and Medium Dulbecco Modified Eagle's minimal essential medium (DMEM) supplemented with 1% penicillin/ Streptomycin (p/s, Gibco, Grand Island, NY, USA) culture medium at 37 °C, 120 rpm for 72 hrs with a standard ratio of 0.2 g/ml of culture medium. After that, the supernatant was withdrawn and centrifuged to prepare the desired extracts, which

were then stored at 4 °C before the cytotoxicity test. A 50×10^3 cells density were cultured in 24-well plates for 24 hrs., then the indirect contact technique was carried out by using the previous extraction medium through an addition of 500 μ l. For the positive control, the cells were cultured with pure medium without any additives while for the negative control, the cells were cultured in presence of 20% dimethyl sulfoxide (DMSO), and different media was changed daily. The cell response against the extraction fluid was evaluated after incubating in a well plate for intervals of 1, 3, and 5 days.

The MTT solution 3-[4,5-dimethylthiazol-2-yl]-2,5- diphenyltetrazolium bromide (MTT; Sigma-Aldrich, St Louis, MO, USA) was prepared in phosphate buffered saline (PBS) at a final concentration of 5 mg/ml. In last of the incubation, 50 μ L of the MTT solution were as added to each well, followed by 4 h of incubation. The medium was aspirated, and 350 μ L of DMSO were added to each well to dissolve the formazan. Thereafter, the absorbance was measured at a 570 nm wavelength using a microplate reader. The live/dead cells staining were performed to determine the viable and non-viable osteoblast cells after 5 days as well as the microscopic images of different samples extraction in media. Live and dead cells were respectively stained with calcein-AM/ethidium Bromide homodimer (Invitrogen) for 30 min at 37 °C and were then imaged using a fluorescence microscope (Olympus, Tokyo, Japan). The cell attachment were observed using scanning electron microscopy (SEM). A 30×10^3 cells were seeded on each surface of the different samples for 48 hrs. Thereafter, 2.5% glutaraldehyde was used to fix cells for 1 h at 4 °C, followed by washing with an ascending series of ethanol (25%, 50%, 75%, and 95 % ethanol) then kept at room temperature, thereafter, SEM images were used to check cell attachment.

2.6 DNA test

The cells were trypsinized at different time intervals and were digested with proteinase K buffer (Sigma-Aldrich, St. Louis, MO) at 56 °C. The DNA was extracted using a NucleoSpin kit (Machery-Nagel GmbH & Co. KG, Germany) according to the manufacturer instructions, and the concentration of the extracted DNA was measured using a NanoDrop spectrophotometer ND-1000 (PepLab, Erlangen, Germany) with a photometric measurement of the optical density at 260 nm.

2.7 Polymerase chain reaction (PCR) analysis

The total RNA was extracted from cells grown on the surface of the different samples and cells cultured in a two-dimensional monolayer (which was used as control). TRIzol solution (Invitrogen) was used according to manufacturer's instructions. A total amount of 1 µg from RNA was used to synthesize the cDNA using random primers and GoScript reverse transcriptase (Promega, Korea). 50 ng of extracted cDNA was used for the PCR analysis with a Professional standard 96 gradient machine (Biometra, Goettingen, Germany). The primer sequences are summarized in **Table 3**. PCR was performed under the following experimental conditions: 94 °C for 3 min, followed by 30 cycles of 94 °C for 30 s, an annealing temperature for 30 s and at 72 °C for 45 s with a final extension at 72 °C for 10 min. The PCR products were analyzed on 1.5% agarose gel stained with ethidium bromide and were visualized with ultraviolet transillumination (G:BOX F3, Syngene, Cambridge, UK) using a 100-base pair DNA ladder as a reference (GeneRuler, Fermentas, Burlington, ON, Canada). Relative gene expression was quantified with Image J software (National Institutes of Health, Bethesda, MD, USA) and GAPDH (Glyceraldehyde 3-phosphate dehydrogenase) was the endogenous control.

2.8 Statistical analysis

Each of the data points from the biological tests in Sections 2.4 represents the (means \pm standard deviations) calculated with at least 3 individual samples. The statistical analysis was conducted using a one-way analysis of variance (one-way ANOVA test). All of the pairwise comparisons were performed with $p < 0.05$ to determine statistical significance. The terms T37, T50, and T80 will refer to different electrolyte temperature at 37 °C, 50 °C, and 80 °C, respectively.

3. Results and discussion

3.1 Surface morphology and phase composition

Fig. 1 shows the FE-SEM images of the bare Mg alloy (control) and the anodized samples at various electrolyte temperatures. The bare sample exhibited grooves as a result of the grinding process, which can be clearly seen in **Fig. 1.a**. The deposition of the anodized film was carried out at a low electrolyte temperature of 37 °C, which is similar to that of human plasma. The surface exhibited random white agglomerates with a nanocactus shape and a nanoplate morphology similar to bone structure, as shown in **Fig. 1.b**. A morphology similar to that of nanoplates could be seen at 50 °C (**Fig. 1.c**). An increase in the electrolyte temperature to 80 °C (**Fig. 1.d**) results in the disappearance of the nanostructure with fewer white particles, and the surface shows a wide porous structure and a decrease in the apatite film affected by the high temperature. The increase in the anodization temperature of the SBF solution revealed that it has an effect on the bicarbonate decomposition on the Mg alloy interface. Hence, the decomposition of bicarbonate ions (HCO_3^-) results in a pH increase in the SBF. Different amounts of bicarbonate

ions are required to reach the critical pH range for apatite formation and to have an effect on the surface morphology of the biomimetic coating⁴⁰. As the temperature increases, the apatite coating with different morphologies can be achieved by varying the pH of the SBF, as shown in the surface morphology in **Fig. 1**. The phase composition of the anodized film was fully investigated using XRD technique, as shown in **Fig. 2**. XRD results indicates Mg peaks observed at ($2\theta=32, 34.5, 47.9, 57.56, 63.2$ and 68.9) with corresponding planes (002,101,102,110 and 102) respectively. In the other hand MgO peaks are appear at ($2\theta=36.5, 72.5,$ and 81.6) with corresponding planes (111, 001, and 222), respectively. Commercial HA peaks are measured to compare with the anodized sample, however, the high HA intensity peak is shown at $2\theta =32 \sim 33$ at which Mg peaks have high intensity located. As a result, it was difficult to detect any apatite peaks which revealed the formation of amorphous apatite formation generated from SBF solution at different temperature in agreement with previous publication³⁵. XPS test was performed to observe the composition of the outer surface of the anodized film, as shown in **Fig. 3**, which indicates that the coated surface is mainly composed of Mg, O, Ca and P elements. The phosphorous (P 2p_{3/2}) peak show low intensity comparing to other elements where inset graph at low peak intensity was shown to indicate the formation of P between 130 and 140 (B.e). The resulting peaks in the XPS measurements reveal the formation of an oxide layer from the MgO and CaP apatite. The detailed XPS elemental analysis peaks are listed in table S1 (Supplementary data) mainly with peaks height (CPS) and At. %. In addition, the supplementary data figure (S1, S2, and S3) show the EDS and EDS element mapping results of the treated samples at temperatures 37 °C, 50 °C, and 80 °C, respectively. The EDS results were selected in two different regions of mostly white colors and gray regions of the samples. At the low white area, a lower percentage of O elements and a high percentage of Mg are present. Conversely, in

the white areas, a higher O percentage and a lower Mg can be seen, which illustrates the formation of oxide particles and apatite. Full scan element mapping and an elemental scan are listed with details of the elemental weight percentage. The apatite film thickness was 7.78 μm , 6.63 μm , and 5.36 μm for T37, T50, and T80 samples, respectively which indicates the decrease of film thickness with increasing electrolyte temperature as it shown in the supplementary data Figure (S4, S5, and S6).

The FTIR spectrum of the different coated samples is shown in fig.4, the band at vibration of (ν_4) assigned to PO_4^{3-} group is located at around 530 cm^{-1} and between (1055-1190) cm^{-1} ⁴¹.

The doublet band at 870 cm^{-1} and band around 1423 cm^{-1} is assigned to CO_3^{2-} group⁴². The strong band vibration around 1635 cm^{-1} and 3350 cm^{-1} are assigned to H_2O ⁴², moreover, the IR band at 3650 cm^{-1} is assigned to O-H in $\text{Mg}(\text{OH})_2$ during the alkaline treatment and hydrated nature of the coating³⁵.

3.2 Surface hydrophobicity

The hydrophilicity of the biomaterials is an important factor that plays an important role in tissue engineering as it affects the initial cell adhesion and proliferation⁴³. **Fig. 5.a** shows the results of water contact angle (CA), the bare sample shows a contact angle of 94°, and the treated samples at different temperatures with angles of 26°, 27°, and 17°, respectively. CA has a great impact on the compatibility of the biomaterials, and it has been found that improving the wettability, i.e., a low contact angle could improve the biocompatibility of the surface^{44, 45}. The cell adhesion to the extracellular matrix (ECM) proteins adsorbed onto the implant interface are highly important to the host response to biomaterials in the tissue-engineering field⁴⁵. Here, the samples treated with anodization at a high electrolytic temperature of 80 °C exhibit a high surface wettability. However, the low apatite formation in the higher temperature lower contact

angle present as there is another factors such as surface roughness and porosity can effect on the surface hydrophilicity.

3.3 Biodegradation behavior

An electrochemical corrosion test using potentiodynamic polarization curves based on tafel slopes in anodic and cathodic reactions was used to assessment the corrosion behavior of the different samples, the test results are summarized in **Table 4**. The bare sample has the lowest resistance to polarization among the samples with $8.26 \pm 3.92 \text{ k}\Omega\cdot\text{cm}^2$ when compared to other samples, which indicates an improvement in the corrosion resistance as a result of the formation of the anodized film in terms of corrosion current and polarization values as shown in **Fig. 5.b** . Moreover, the Nyquist plot in **Fig. 6.a** shows a high inductive loop at an electrolyte temperature of 37 °C, followed by a decrease in the loop diameter at 50 °C and 80 °C. The Bode diagram in **Fig. 6.b** revealed an improvement in the corrosion resistance that was in agreement with the results of the Nyquist plot. The anodized film as a form of surface protection is analyzed using an equivalent circuit for the resulting Nyquist plot, as shown in **Fig. 7**. The resulting data was fitted with a standard equivalent circuit in a bare simple circuit with three components, as illustrated in the circuit in **fig. 7.a** (a): The corrosive solution resistance R_s , passive layer resistance (R), and capacitance (C). However, the other side exhibits a coated layer with two parallel resistance (R_2) and total capacitive (Q_2) as shown in **fig.7.b** the dense inner layer and pours outer layer. Line EDS results are shown in supplementary data (figure. S7), EDS result show elemental distribution through the two anodizing layers. The relevant equivalent circuit parameters are shown in **Table 5**, the coating charge resistance can be shown to have a high

value at T37 with 21.91 k.Ω, which may be due to the decrease in the oxide layer thickness that resulted from the temperature increase. The EIS results find an improvement could be represented in the capacitance loop diameters which higher than that of electrodeposition of HA in Mg alloy ⁷.

Fig.8 (a-c) show SEM images of the anodized samples after 3 days of incubation in alph MEM media with MC3T3-E1 cells to mimic the host environment with implant materials. The results show a nanoplates growth in well order which enhance surface bioactivity and mimic nanoplates structure similar to that of bone leading to stimulate specific cellular responses at the molecular level ⁴¹. Growth of such nanoplates during biomineralization at presence of biomolecules can significantly modify the growth rates of the mineralizing crystal. The different charges in basal plane of HA is rich in OH⁻ ions where positive in the prism plane which rich with Ca⁺². As a results, interaction of biomolecules with new surface at different charges play a role in the nucleation and growth of HA during the biomineralisation ⁴⁶. In addition, immersion test results are shown in Fig.8 (d), the weight loss of different samples with compared to the bare ones are displayed. The histogram indicate that after 5 days of immersions small differences in mass loss of the sample groups, however, after 10 and 15 days of immersion bare sample show higher mass loss compared to the anodized samples. The standard electrochemical Mg is -2.4 V and -1.5 in an aqueous solution due to the formation of the Mg(OH)₂ layer ⁴⁷.The low difference in the corrosion resistance values between the naked sample and the anodized samples is due to the penetration of corrosive chloride Cl⁻ ions to the thin film of apatite which are closed to each other with maximum values of 7.78 μm on the Mg alloy surface ⁴. Moreover, the labile ions on bone-like apatite crystals (PO₄⁻³, HPO₄⁻², and CO₃⁻²) did not dissolve in the physiologic solution and behave as corrosion- resistant material, thus gaining more weight from the corrosion product ⁴⁸.

This was revealed by the growth of biomineralization nanoplates in α -MEM media at 37 °C as shown in **fig.8**, such morphology is exist in the natural bone nanocrystals in a plate-like shape with a length of 30–200 nm and a thickness of 2–7 nm.

3.4 In vitro osteoblast cell responses

The cell viability is investigated to evaluate the biocompatibility of the biomaterials *in vitro*. **Fig. 9.a** shows the MTT absorbance of the different samples after 1, 3, and 5 days of incubation with different samples. The proliferation in the T80 samples group has the highest hFOB 1.19 cell lines proliferation among the different samples. The osteoblast cells proliferated on the anodized samples showing time-dependent behavior, and the sample group with the same culture time shows significant values with $p < 0.05$. The different culture groups in a time dependent scenario have a significant values at α level of 0.05 where $p < 0.05$. The bare sample exhibits a low absorbance throughout the culture time when compared to the anodized ones. The cell morphology after five days of cultures in **fig.9** (b,c,d,e) show more cell proliferation comparing to the bare sample which coincident with the MTT results. **Fig. 10** shows the live/dead cells fluorescence analysis to examine the bone cell proliferation, cell viability for the positive control, negative control, bare sample, T37, T50, and T80. The microscopic images reveal a healthy cell morphology in all groups after the fifth day. However, the bare samples exhibit a low cell density relative to the anodized samples which have a significantly higher cell density. Furthermore, the cells can be seen to have elongated in the same direction with multiple layers of cells in different anodized samples. Thus the results shown in **Fig. 10.f** are in agreement with the MTT tests, which show the highest cell viability for the T-80 samples. The interaction of biomaterials interface and cells is important issue as it is responsible for cell adhesion and proliferation. Cells

attachment with the bare samples and new surface were confirmed using SEM images as shown in **fig.11**. The bare sample show a few cells due to smooth surface thus, cells tend to migrate, and in the other side the treated samples show significant change. The morphology of the cells was observed to be intermediate between flat and spherical shape due to the porosity of the apatite film. The results indicate a good adhesion for the osteoblast cells with the treated samples.

A quantification of the DNA test was performed as an indicator of the cell proliferation from wells containing HFOB cells in the presence of conditioned media, which shows an increase in the amount of DNA from day 1 to day 5 for different samples, as shown in **Fig. 12**. The results indicate that the anodized samples have a high percentage of DNA concentration over various culture days. The expressions of mRNA markers related to bone tissue formation, including OC, OP, and COL-1, were evaluated by densitometric analysis of the PCR products to compare the osteogenic potential of the hFOB grown on the different materials, as shown in **Fig. 13**. The difference in the expression of osteocalcin (OC) and osteopontin (OP) was not significant in cells grown on AZ31B Mg alloys prepared at different levels of electrolyte temperature, while their expressions were higher than the expression of cells grown on the bare Mg alloys or in a culture dish. This indicates that the bioactive films significantly increased the osteoblast cell function, such as the ECM mineralization, cell adhesion, and bone remodeling. The expression of collagen I (Col-I) was higher in alloys prepared at 50 °C, which may be explained to be the cell response to an increase in cell attachment toward the apatite film. The OC and OP are osteoblast-specific marker genes with OC as a major non-collagenous protein component of bone extracellular matrix (ECM) produced by both osteoblasts and osteoclasts. OP is commonly found in specific regions of the bone *in vivo*, such as in cement lines in remodeled bone, and it is involved in bone remodeling, cell adhesion, and ECM mineralization. *In vitro*, osteopontin is commonly

associated with the formation of a collagen-free cement layer on which bone is subsequently deposited. Collagen I aids in the deposition of collagen, the most abundant ECM protein in bone.

The results support our hypothesis that these are biocompatible coating materials with improved surface bioactivity. In addition, the osteoblast cell function was examined using both untreated and treated samples. OC and OP are osteoblast-specific marker genes, where OC is a major non-collagenous protein component of bone extracellular matrix (ECM) produced by both osteoblasts and osteoclasts and OP is commonly found in specific regions of bone *in vivo*, such as cement lines in remodeling bone. OP is involved in bone remodeling, cell adhesion, and ECM mineralization. *In vitro*, osteopontin is commonly associated with the formation of a collagen-free cement layer on which bone is subsequently deposited. On the other hand, Collagen I aids in the deposition of collagen, which is the most abundant ECM protein in bone⁴⁹. The present results thus indicate that all cells grown on coated materials showed upregulated expression of OC and OP relative to bare alloys or cells cultured on tissue culture dish, which may indicate the efficient apatite coating of Mg alloys. Based on the above results, the temperature of the anodization electrolyte can be concluded to have increased the porosity of the output oxide film and decreased the CaP particle content, which are the main component of apatite, as can be observed in the samples from the 37 °C and 50 °C electrolytic temperature with a nanostructure formation⁵⁰⁻⁵².

4. Conclusions

In summary, a simple one step method was implemented to generate bone-like apatite with a nanoplates morphology on the AZ31B Mg alloy using SBF solution as an electrolyte in anodization process. The results show the formation of apatite film at different anodization electrolyte temperature within a short time by accelerating the apatite formation by means of

anodization parameters. The thin film was fully characterized with slightly improvements in corrosion resistance due to thin thickness with an advantage of formation of a unique morphology similar to bone structure in a similar biological environment. Moreover, the biomimetic apatite film under the electrolyte temperature in the range from 37 to 50 °C exhibits minor differences in alloy degradation, morphology and biological response in the MTT test. The results find that, in addition to the enhancement of cell proliferation, the apatite film promoted osteoblastic differentiation of hFOB 1.19 cell lines in vitro by upregulating osteogenic gene expression. Moreover, the proposed method not only improve the bioactivity and corrosion resistance but also introduce a unique structure before and after short time of implantation thus it could help the implant material to engage with the bone tissue and eliminated the induced stress shield effect.

Acknowledgment

This paper was supported by grant from the Basic Science Research Program through National Research Foundation of Korea (NRF) by Ministry of Education, Science and Technology (Project no NRF-2015R1C1A1A02036404). And also partially supported by the Human Resource Training Program for Regional Innovation and Creativity through the Ministry of Education and National Research Foundation of Korea (NRF-2015H1C1A1035635).

References

1. F. Witte, *Acta Biomaterialia*, 2010, 6, 1680-1692.
2. M. Razavi, M. Fathi, O. Savabi, S. Mohammad Razavi, B. Hashemi Beni, D. Vashae and L. Tayebi, *Materials Letters*, 2013, 113, 174-178.
3. G. Song, *Advanced Engineering Materials*, 2005, 7, 563-586.
4. M. P. Staiger, A. M. Pietak, J. Huadmai and G. Dias, *Biomaterials*, 2006, 27, 1728-1734.
5. X. Zhang, X.-W. Li, J.-G. Li and X.-D. Sun, *ACS Applied Materials & Interfaces*, 2014, 6, 513-525.
6. M. A. Fernandez-Yague, S. A. Abbah, L. McNamara, D. I. Zeugolis, A. Pandit and M. J. Biggs, *Advanced Drug Delivery Reviews*, 2015, 84, 1-29.
7. Y. W. Song, D. Y. Shan and E. H. Han, *Materials Letters*, 2008, 62, 3276-3279.
8. E. Zhang, L. Xu and K. Yang, *Scripta Materialia*, 2005, 53, 523-527.

9. T. S. N. Sankara Narayanan, I. S. Park and M. H. Lee, *Progress in Materials Science*, 2014, 60, 1-71.
10. S. V. Lamaka, M. F. Montemor, A. F. Galio, M. L. Zheludkevich, C. Trindade, L. F. Dick and M. G. S. Ferreira, *Electrochimica Acta*, 2008, 53, 4773-4783.
11. C. Blawert, W. Dietzel, E. Ghali and G. Song, *Advanced Engineering Materials*, 2006, 8, 511-533.
12. A. Zomorodian, M. P. Garcia, T. Moura e Silva, J. C. S. Fernandes, M. H. Fernandes and M. F. Montemor, *Acta Biomaterialia*, 2013, 9, 8660-8670.
13. L. Chai, X. Yu, Z. Yang, Y. Wang and M. Okido, *Corrosion Science*, 2008, 50, 3274-3279.
14. H. M. Mousa, K. H. Hussein, H. M. Woo, C. H. Park and C. S. Kim, *Ceramics International*, 2015, 41, 10861-10870.
15. H. M. Mousa, D. H. Lee, C. H. Park and C. S. Kim, *Applied Surface Science*, 2015, 351, 55-65.
16. A. F. Yetim, *Surface and Coatings Technology*, 2010, 205, 1757-1763.
17. S. Hiromoto, T. Shishido, A. Yamamoto, N. Maruyama, H. Somekawa and T. Mukai, *Corrosion Science*, 2008, 50, 2906-2913.
18. D. Xue, Y. Yun, M. J. Schulz and V. Shanov, *Materials Science and Engineering: C*, 2011, 31, 215-223.
19. L. Zhu, Y. Li and W. Li, *Surface and Coatings Technology*, 2008, 202, 5853-5857.
20. S. Thelen, F. Barthelat and L. C. Brinson, *Journal of Biomedical Materials Research Part A*, 2004, 69A, 601-610.
21. W.-Q. Yan, M. Oka and T. Nakamura, *Journal of Biomedical Materials Research*, 1998, 42, 258-265.
22. P. Ducheyne and Q. Qiu, *Biomaterials*, 1999, 20, 2287-2303.
23. D. A. Puleo and A. Nanci, *Biomaterials*, 1999, 20, 2311-2321.
24. A. A. Sawyer, K. M. Hennessy and S. L. Bellis, *Biomaterials*, 2005, 26, 1467-1475.
25. S. Radin and P. Ducheyne, *Journal of Biomedical Materials Research*, 1996, 30, 273-279.
26. S. Hiromoto and A. Yamamoto, *Electrochimica Acta*, 2009, 54, 7085-7093.
27. M. Tomozawa and S. Hiromoto, *Applied Surface Science*, 2011, 257, 8253-8257.
28. C. Wen, S. Guan, L. Peng, C. Ren, X. Wang and Z. Hu, *Applied Surface Science*, 2009, 255, 6433-6438.
29. K. S. Vecchio, X. Zhang, J. B. Massie, M. Wang and C. W. Kim, *Acta Biomaterialia*, 2007, 3, 910-918.
30. G. Y. Pettis, L. B. Kaban and J. Glowacki, *Journal of Oral and Maxillofacial Surgery*, 1990, 48, 1068-1074.
31. O. Suzuki, S. Kamakura, T. Katagiri, M. Nakamura, B. Zhao, Y. Honda and R. Kamijo, *Biomaterials*, 2006, 27, 2671-2681.
32. T. Kokubo, H.-M. Kim and M. Kawashita, *Biomaterials*, 2003, 24, 2161-2175.
33. F. Li, Q. L. Feng, F. Z. Cui, H. D. Li and H. Schubert, *Surface and Coatings Technology*, 2002, 154, 88-93.
34. X. Lu and Y. Leng, *Biomaterials*, 2005, 26, 1097-1108.
35. A. Cuneyt Tas, *Journal of Non-Crystalline Solids*, 2014, 400, 27-32.
36. S. Keim, J. G. Brunner, B. Fabry and S. Virtanen, *Journal of Biomedical Materials Research Part B: Applied Biomaterials*, 2011, 96B, 84-90.
37. L. Jonášová, F. A. Müller, A. Helebrant, J. Strnad and P. Greil, *Biomaterials*, 2004, 25, 1187-1194.
38. P. Li, *Journal of Biomedical Materials Research Part A*, 2003, 66A, 79-85.
39. H. M. Mousa, K. H. Hussein, H. R. Pant, H. M. Woo, C. H. Park and C. S. Kim, *Colloids and Surfaces A: Physicochemical and Engineering Aspects*, 2016, 488, 82-92.
40. H. Qu and M. Wei, *Journal of Biomedical Materials Research Part B: Applied Biomaterials*, 2008, 87B, 204-212.

41. H. M. Mousa, A. P. Tiwari, J. Kim, S. P. Adhikari, C. H. Park and C. S. Kim, *Materials Letters*, 2016, 164, 144-147.
42. A. Farzadi, F. Bakhshi, M. Solati-Hashjin, M. Asadi-Eydivand and N. A. a. Osman, *Ceramics International*, 2014, 40, 6021-6029.
43. M. Cheng, J. Deng, F. Yang, Y. Gong, N. Zhao and X. Zhang, *Biomaterials*, 2003, 24, 2871-2880.
44. N. P. Desai and J. A. Hubbell, *Journal of Biomedical Materials Research*, 1991, 25, 829-843.
45. R. Tzoneva, N. Faucheux and T. Groth, *Biochimica et Biophysica Acta (BBA) - General Subjects*, 2007, 1770, 1538-1547.
46. B. Viswanath and N. Ravishankar, *Biomaterials*, 2008, 29, 4855-4863.
47. R. Ambat, N. N. Aung and W. Zhou, *Corrosion Science*, 2000, 42, 1433-1455.
48. H.-M. Kim, Y. Kim, S.-J. Park, C. Rey, L. HyunMi, M. J. Glimcher and J. Seung Ko, *Biomaterials*, 2000, 21, 1129-1134.
49. N. Zhao and D. Zhu, *PLoS ONE*, 2014, 9, e110420.
50. T. Aerts, T. Dimogerontakis, I. De Graeve, J. Fransaer and H. Terryn, *Surface and Coatings Technology*, 2007, 201, 7310-7317.
51. S. Theohari and C. Kontogeorgou, *Applied Surface Science*, 2013, 284, 611-618.
52. F.-H. Lin, Y.-S. Hsu, S.-H. Lin and J.-S. Sun, *Biomaterials*, 2002, 23, 4029-4038.

Figure caption

- Fig.1 Fig.1 FE-SEM images of the different samples: (a) bare sample, (b) T37, (c) T50, and (d) T80.
- Fig.2 XRD patterns of the different samples under different anodization conditions: (a) Commercial HA powder (b) T37, (c) T50, (d) T80.
- Fig.3 XPS spectra of the treated samples using anodization: (a) T37, (b) T50, and (c) T80. The inset image show scan region at p 2p_{3/2} due to the low intensity.
- Fig.4 FT-IR spectra the different anodized samples at different electrolytic temperature.
- Fig.5 (a) Water contact angle of the different samples: Bare sample, T37, T50, and T80, b) potentiodynamic polarization curve of the anodized samples with a comparison to bare sample as control.
- Fig.6 EIS result: (a) Nyquist plot of the different AZ31B Mg samples, (b) Bode plot of the different samples.
- Fig.7 Illustrative diagrams show different equivalent circuit of: (a) the bare samples, (b) anodized samples.
- Fig.8 Figure show SEM images of apatite morphology nucleation after immersion in α -MEM media incubated at 37°C and humidity 95 % for three days in the different samples (a) T37, (b) T50, and (c) T80. Histogram in (d) shows mass losses in the

different samples compared with the bare sample as control, test was performed at different intervals of times.

- Fig.9 (a) HFOB 1.19 cell proliferation versus culture days of the negative control, bare sample, T37, T50, T80, and positive control, (b, c, d, e) cell proliferation after five days. Statistical analysis was performed, and the data are presented as (means \pm standard deviations, n=4 samples). The significant differences were calculated using a one-way ANOVA test at $\alpha = 0.05$, Asterisks (*) indicates $p < 0.05$ comparing to bare sample.
- Fig.10 Microscopic florescent images for the live / dead cells of the a) negative control, b) positive control, c) bare sample, d) T37, e) T50, f) T80.
- Fig.11 SEM images of the cell attachment on the different samples after two days of culture.
- Fig.12 DNA test of the different samples among the culture days, the data are presented as (means \pm standard deviation) and n=3 samples. The significant difference in the present data was calculated based on an ANOVA one way test with a confidence interval of $\alpha = 0.05$.
- Fig.13 (a) Gel electrophoresis of the PCR products of the different samples on 1.5% agarose, followed by analysis of bands density using Image J software (b).

Table caption

- Table 1. Chemical composition of the AZ31B magnesium alloy in terms of weight percentage (wt. %).
- Table.2 Ions concentrations of SBF in comparison with ions concentrations in human blood plasma.
- Table.3 Primer sequence used for the PCR analysis
- Table .4 Potentdynamic polarization test parameters results. Data are presented with means \pm standard deviation.
- Table .5 EIS equivalent circuit parameters results.

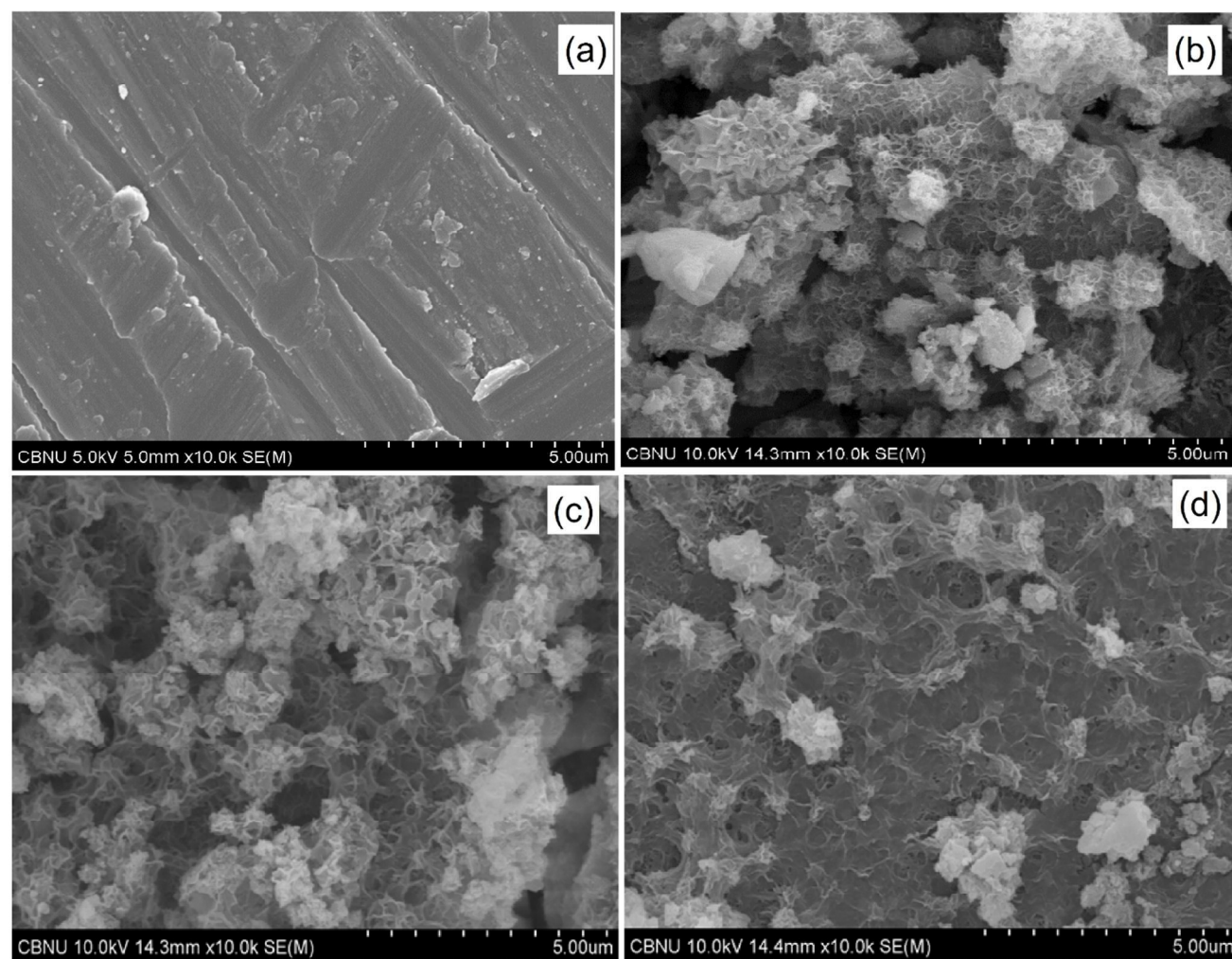


Fig.1 FE-SEM images of the different samples: (a) bare sample, (b) T37, (c) T50, and (d) T80.

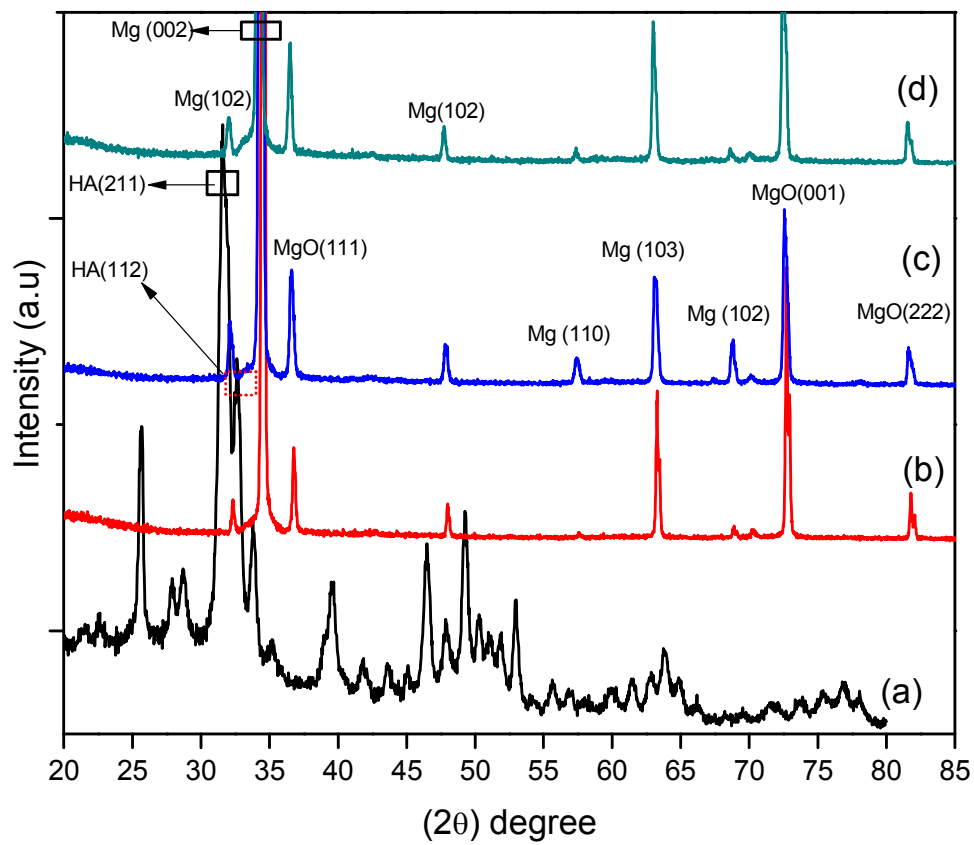


Fig.2 XRD patterns of the different samples under different anodization conditions: (a) Commercial HA powder (b) T37, (c) T50, (d) T80.

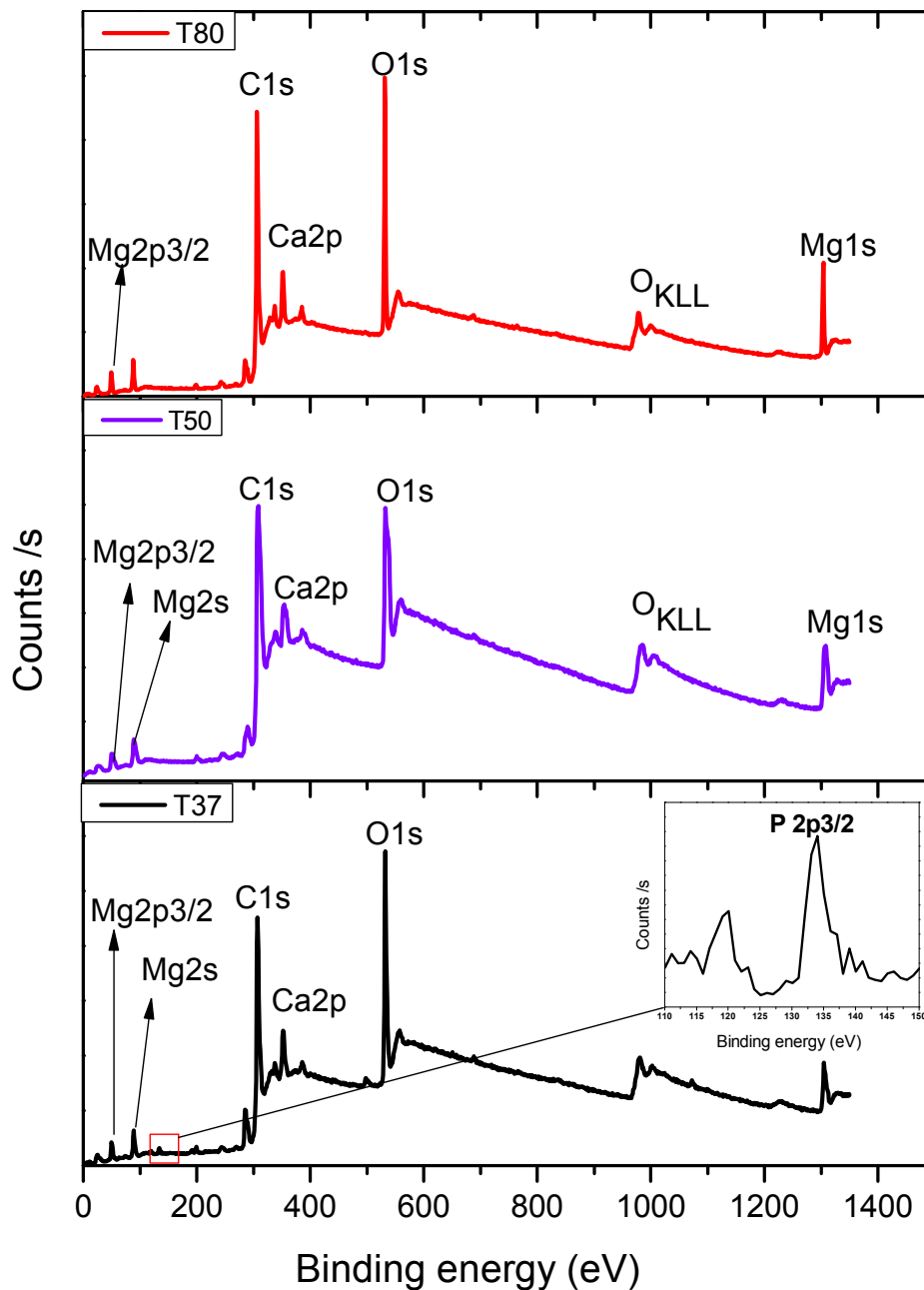


Fig.3 XPS spectra of the treated samples using anodization: (a) T37, (b) T50, and (c) T80. The inset image show scan region at p 2p3/2 due to the low intensity.

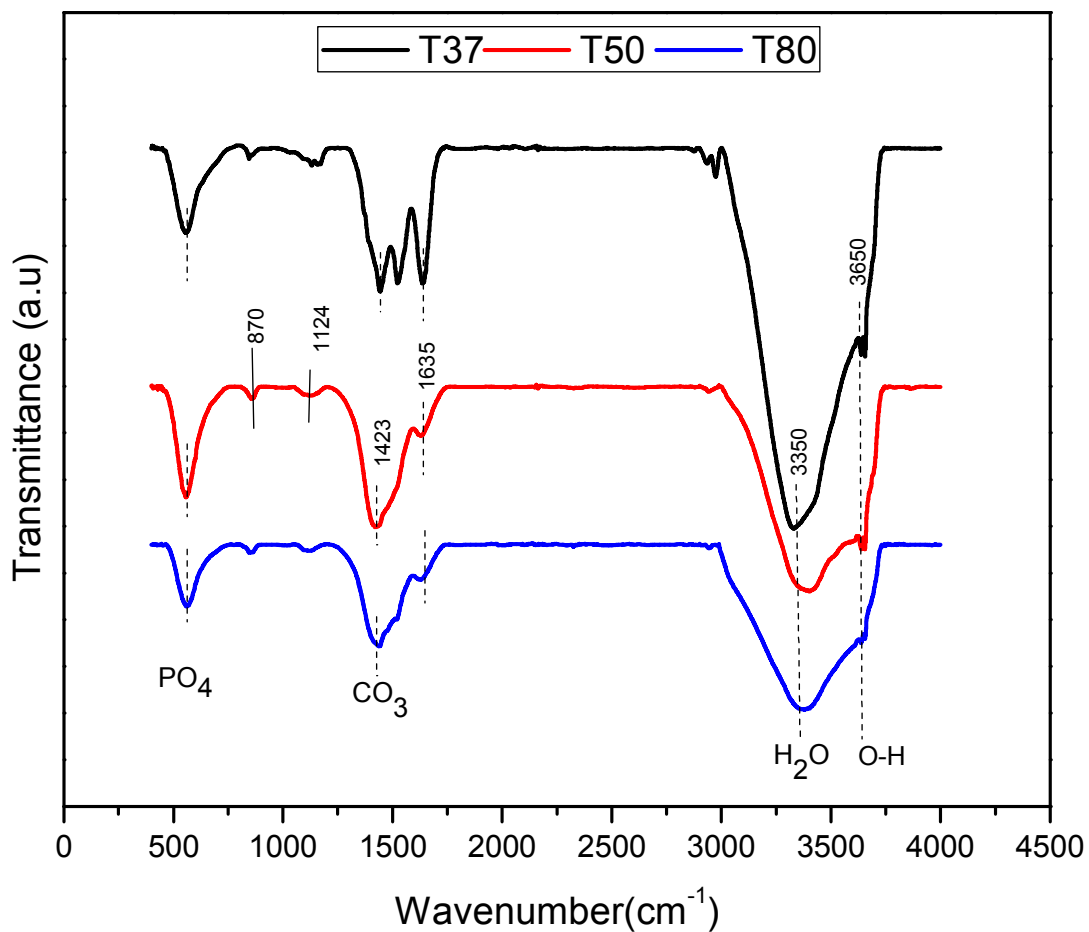


Fig.4 FT-IR spectra the different anodized samples at different electrolytic temperature.

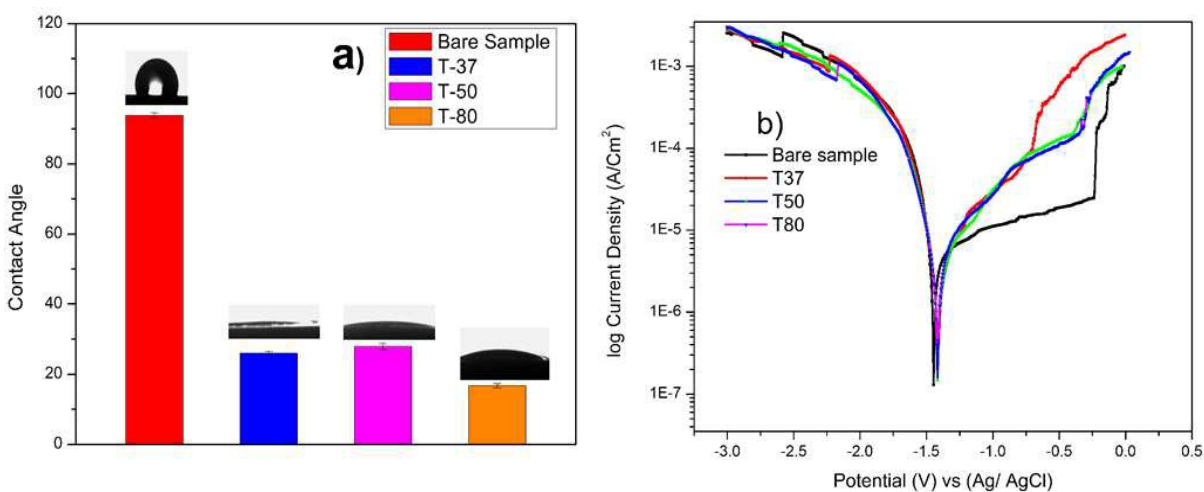


Fig.5: (a) Water contact angle of the different samples comparing to bare one. (b) potentiodynamic polarization curve of the anodized samples with a comparison to bare sample as control.

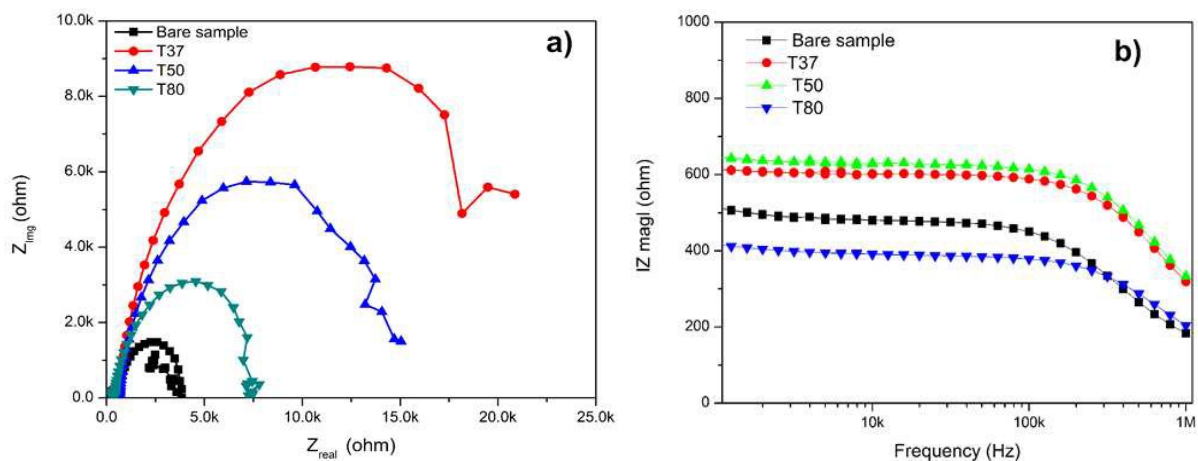


Fig.6 : EIS result: (a) Nyquist plot of the different AZ31B Mg samples, (b) Bode plot of the different samples.

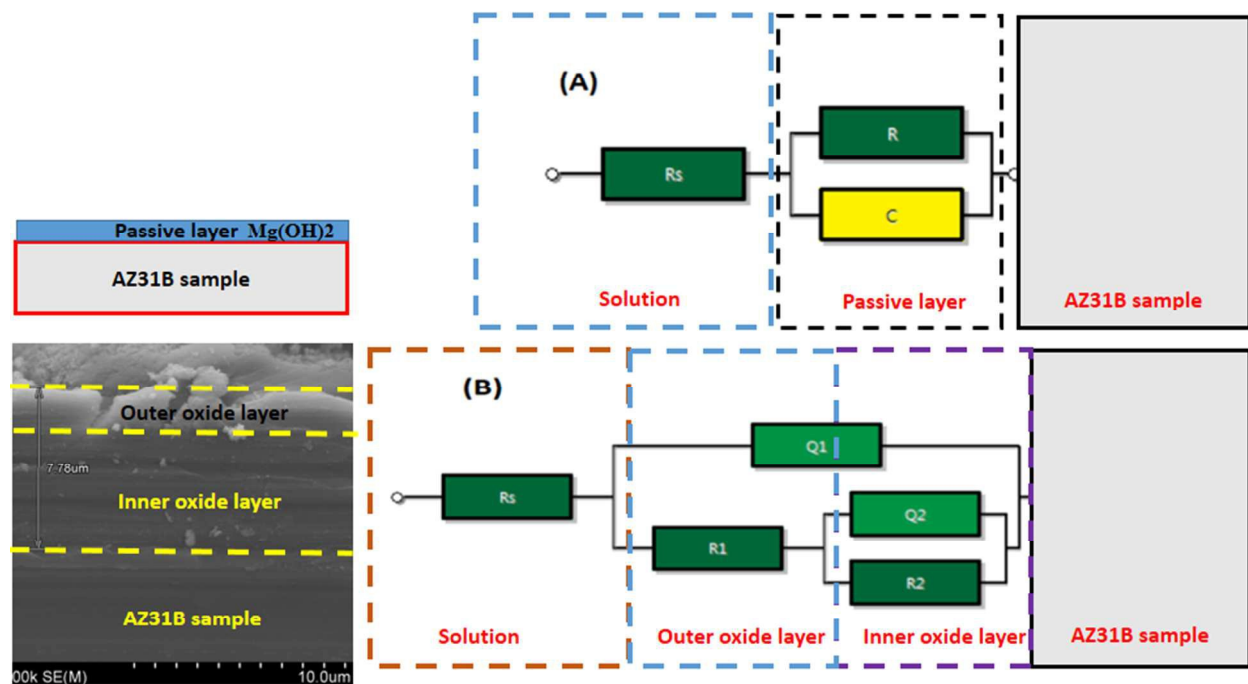


Fig.7. Illustrative diagrams show different equivalent circuit of: (a) the bare samples, (b) anodized samples.

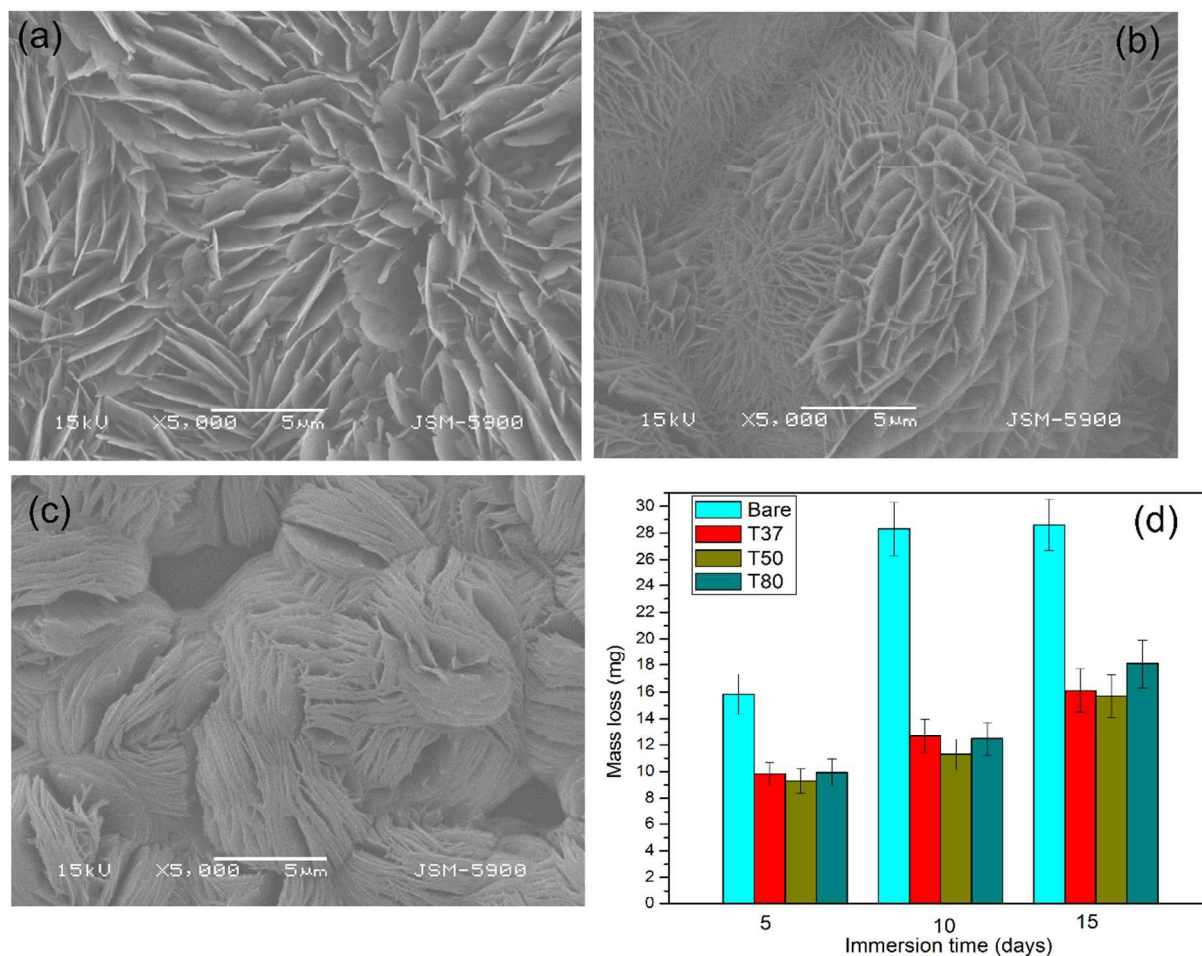


Fig.8 Figure show SEM images of apatite morphology nucleation after immersion in α -MEM media incubated at 37°C and humidity 95 % for three days in the different samples (a) T37, (b) T50, and (c) T80. Histogram in (d) shows mass losses in the different samples compared with the bare sample as control, test was performed at different intervals of times.

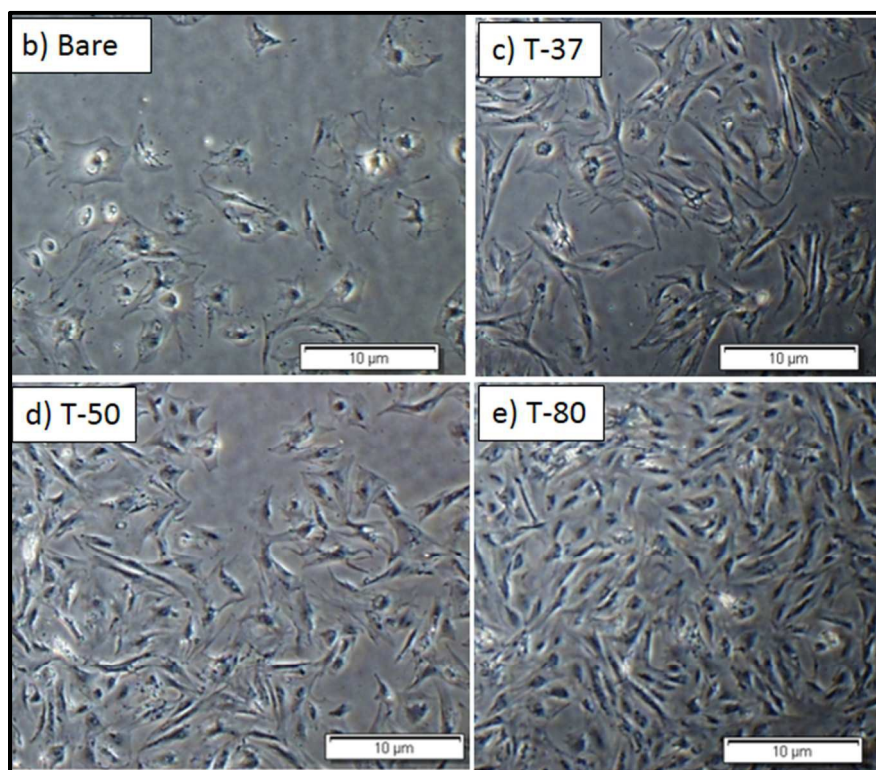
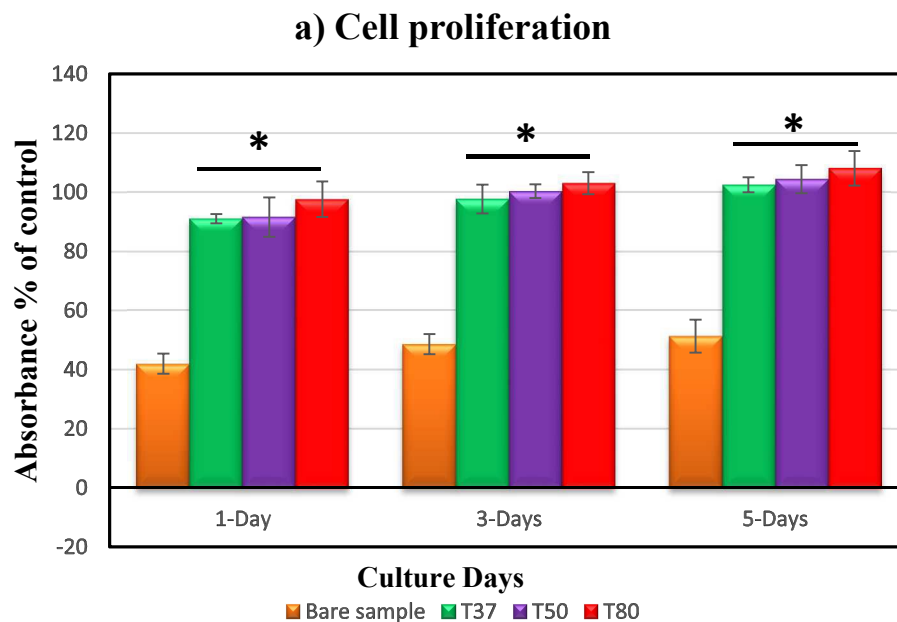


Fig.9: (a) HFOB 1.19 cell proliferation versus culture days of the negative control, bare sample, T37, T50, T80, and positive control, (b, c, d, e) cell proliferation after five days. Statistical analysis was performed, and the data are presented as (means \pm standard deviations, $n=4$ samples). The significant differences were calculated using a one-way ANOVA test at $\alpha = 0.05$, Asterisks (*) indicates $p < 0.05$ comparing to bare sample.

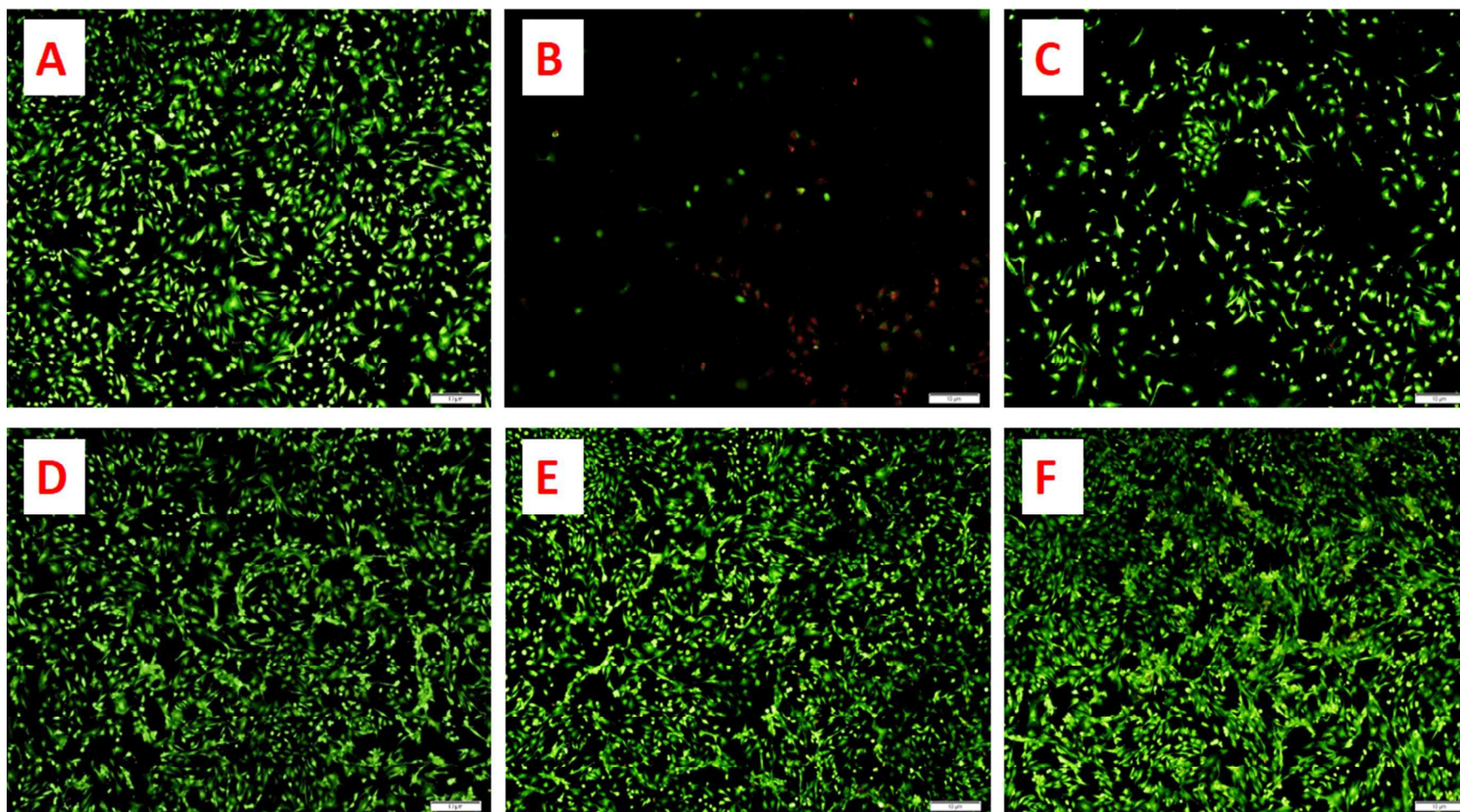


Fig.10 Microscopic florescent images for the live / dead cells of the a) negative control, b) positive control, c) bare sample, d) T37, e) T50, f) T80.

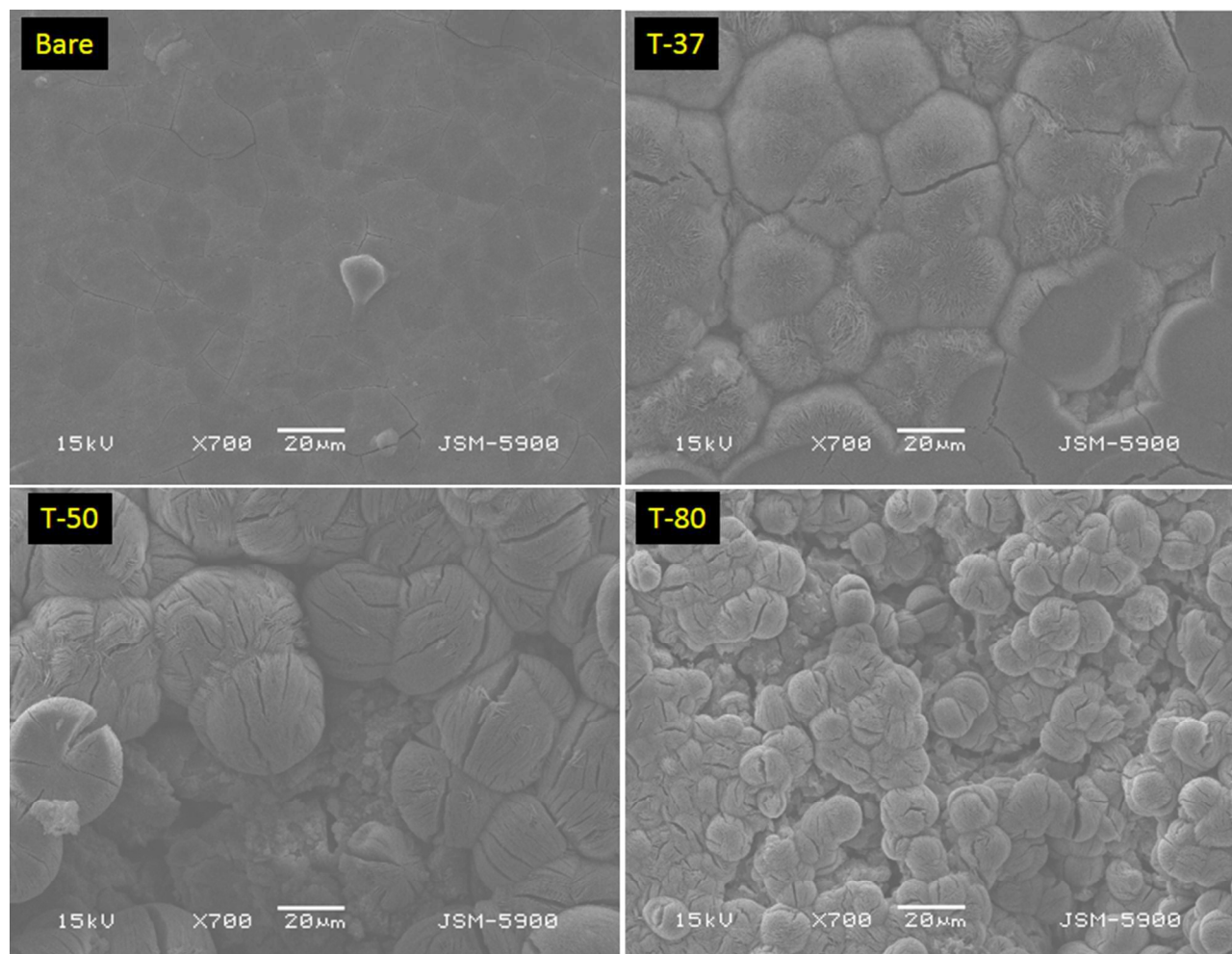


Fig.11 SEM images of the cell attachment on the different samples after two days of culture

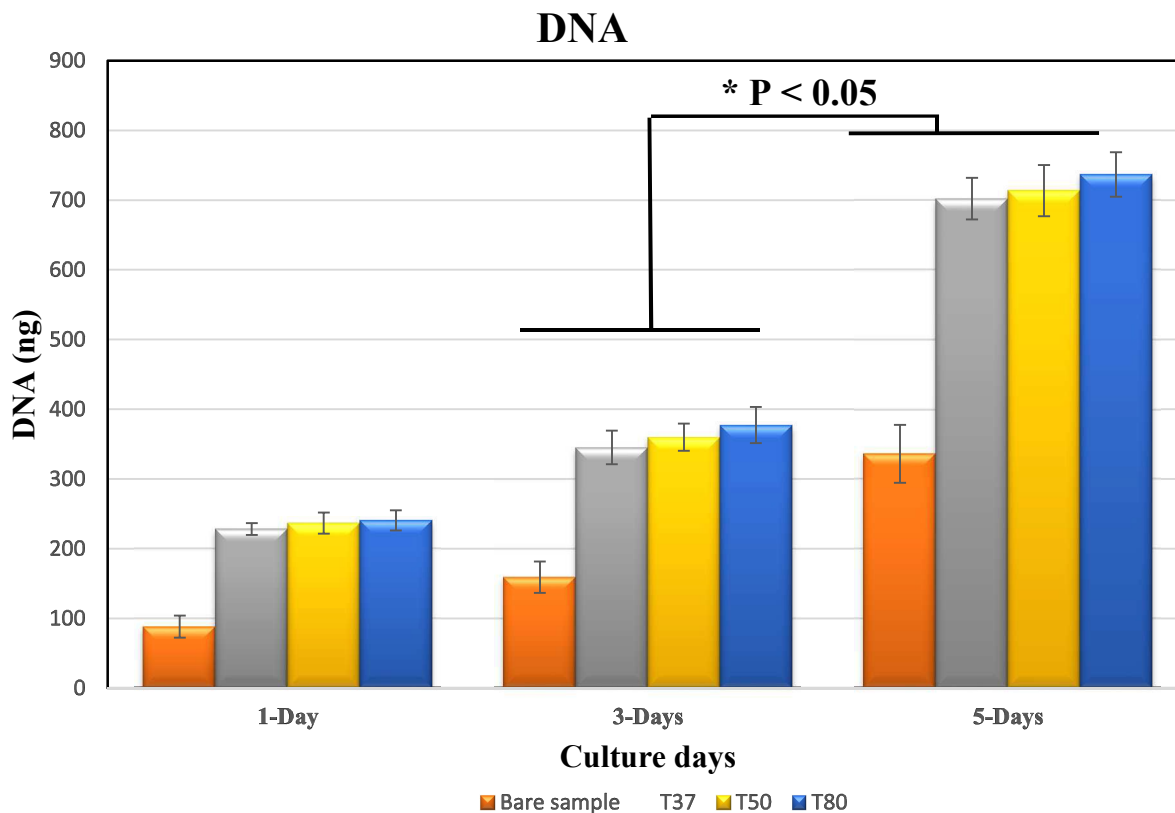


Fig.12 DNA test of the different samples among the culture days, the data are presented as (means \pm standard deviation) and $n=3$ samples. The significant difference in the present data was calculated based on an ANOVA one way test with a confidence interval of $\alpha = 0.05$.

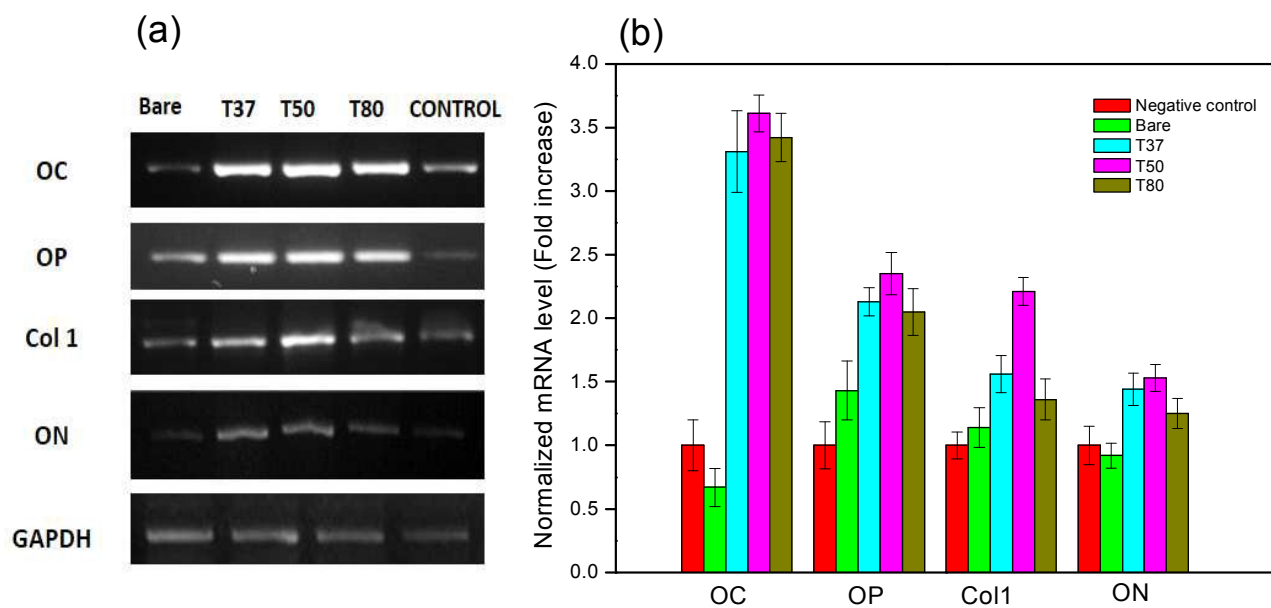


Fig.13 (a) Gel electrophoresis of the PCR products of the different samples on 1.5% agarose, followed by analysis of bands density using Image J software (b).

Table 1. Chemical composition of the AZ31B magnesium alloy in terms of weight percentage (wt. %).

Element	Al	Zn	Mn	Si	Cu	Mg
(Wt. %)	2.5-3.5	0.7-1.3	0.2-1.0	0.05	0.01	Balance

Table.2 Ions concentrations of SBF in comparison with ions concentrations in human blood plasma

	Ions concentration (mM)								pH
	Na ⁺	K ⁺	Mg ⁺²	Ca ⁺²	Cl ⁻	HCO ₃ ⁻	HPO ₄ ⁻²	SO ₄ ⁻²	
Human blood plasma	142.0	5.0	1.5	2.5	103.0	27.0	1.0	0.5	7.2-7.4
SBF	142.0	5.0	1.5	2.5	147.0	4.2	1.0	0.5	7.4

Table.3 Primer sequence used for the PCR analysis

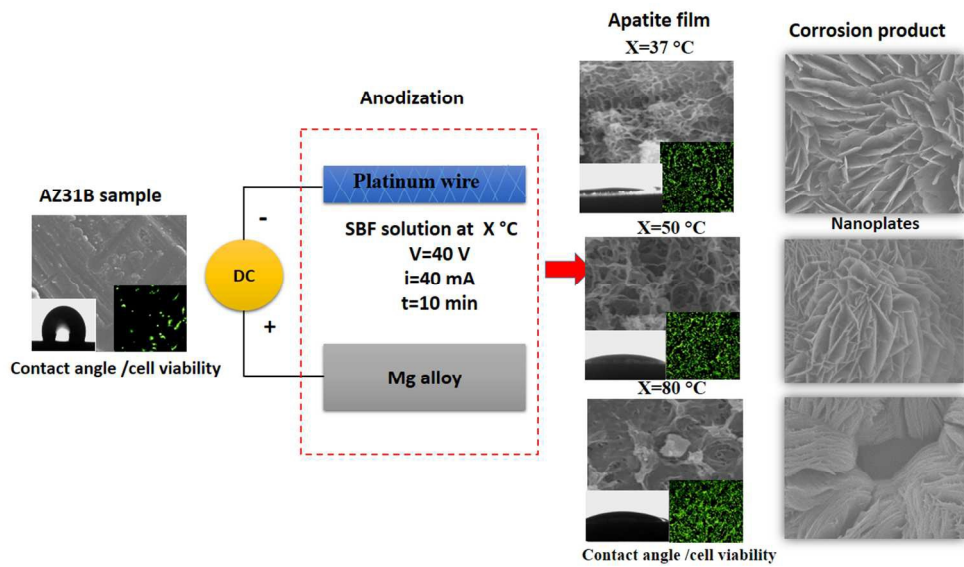
Primer	Primer sequences		Annealing temperature
	Forward	Reverse	
Osteocalcin	5'- ACA CTC CTC GCC CTA TTG -3'	5'- GAT GTG GTC AGC CAA CTC -3'	59.3
Osteopontin	5'- CTC AGG CCA GTT GCA GCC -3'	5'- CAA AAG CAA ATC ACT GCA ATT CTC -3'	61.4
Collagen I	5'- CAG CCG CTT CAC CTA CAG C -3'	5'- TTT TGT ATT CAA TCA CTG TCT TGC C -3'	57.1
Osteonectin	5'- CTC GGT GTG GGA GAG GTA CC -3'	5'- CTC AGG CCA GTT GCA GCC -3'	59.4
GAPDH	5'-ACA GTC AGC CGC ATC TTC TT-3'	5'-GAC AAG CTT CCC GTT CTC AG-3'	59.7

Table .4 Potentdynamic polarization test parameters results. Data are presented with means \pm standard deviation.

	E_{corr} (V)	I_{corr} ($\mu\text{A}/\text{Cm}^2$)	R_p ($\text{K}\Omega.\text{Cm}^2$)
AZ31B-control	-1.46 \pm 0.016	2.796 \pm 1.54	8.257 \pm 3.92
T-37	-1.422 \pm 0.011	3.5125 \pm 0.21	11.9925 \pm 1.62
T-50	-1.415 \pm 0.001	2.105 \pm 0.007	13.8565 \pm 0.73
T-80	-1.412 \pm 0.007	3.5115 \pm 0.304	12.071 \pm 0.17

Table .5 EIS equivalent circuit parameters results.

	R_s (Ω)	R ($\text{K}\Omega$)	C (μ)	R_1 ($\text{k}\Omega$)	Q_1 (m)	R_2 ($\text{k}\Omega$)	Q_2
Substrate	351.95	2.51	2.62	-	-	-	-
T37	526.77	-	-	21.91	848.62	21.92 k	222a
T50	546.5	-	-	14.66	831	14.65k	222a
T80	324	-	-	6.85	705.6	404.47G	-715.1m



338x190mm (96 x 96 DPI)